Nano Research

ISSN 1998-0124 CN 11-5974/O4
https://doi.org/10.26599/NR.2026.94909140

Research Article

2D TiN/graphene metacomposite for photosynthesis-inspired EM modulation and multi-stage attenuation

Yi Zhang, Lu Zhang, Menghan Zhang, Yaqin Ding, Kailin Feng, Lei Zhang, Cuiping Li, Chunhong Gong(✉)
National & Local Joint Engineering Research Center for Applied Technology of Hybrid Nanomaterials, College of Chemistry and Molecular Sciences, Henan University, Kaifeng 475004, China

Nano Res., **Just Accepted Manuscript** • https://doi.org/10.26599/NR.2026.94909140
https://www.sciopen.com/journal/1998-0124 on Aug. 22, 2026

Just Accepted

TABLE OF CONTENTS (TOC)

2D TiN/Graphene Metacomposite for Photosynthesis-Inspired EM Modulation and Multi-Stage Attenuation

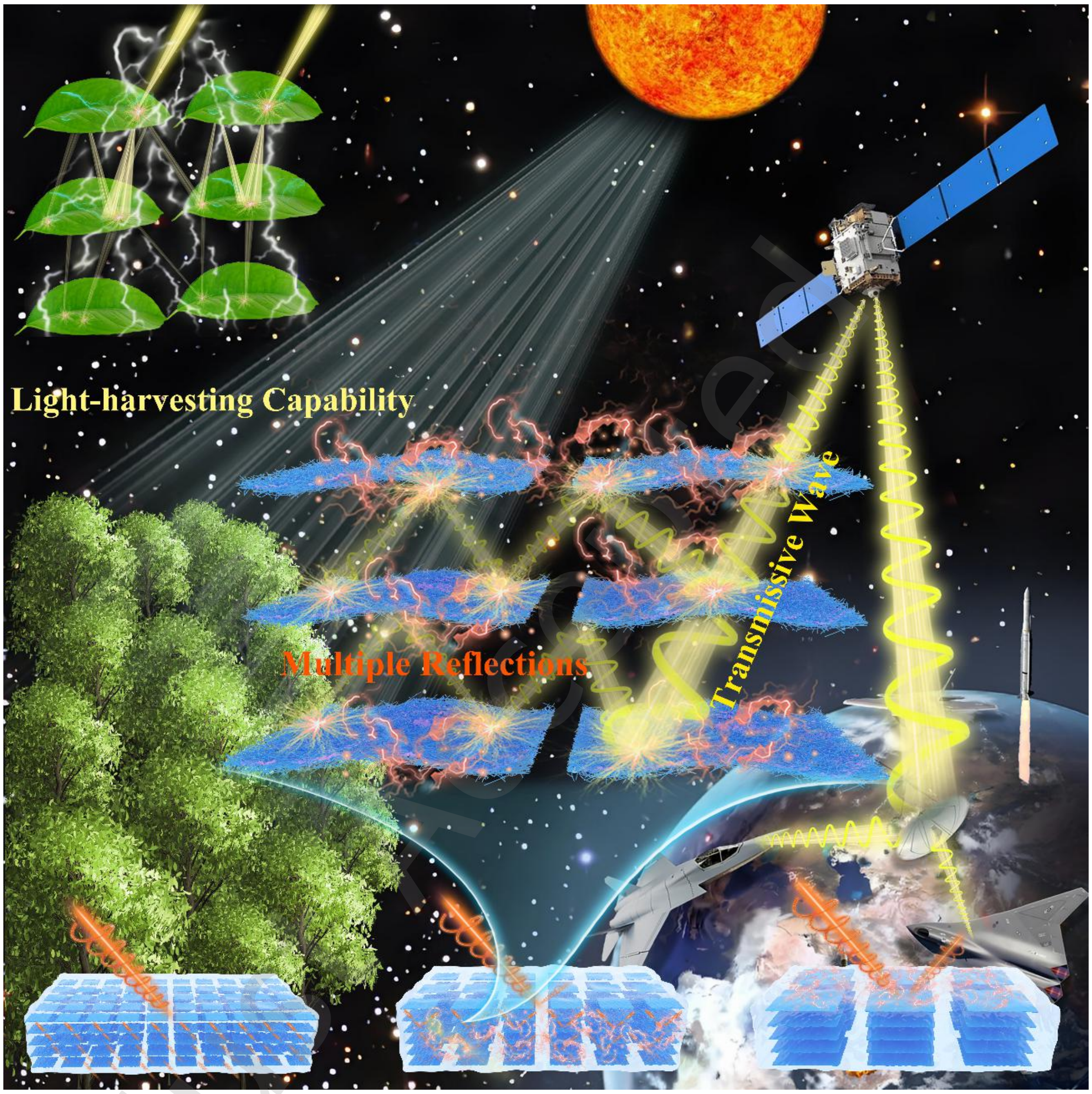

Leaf-inspired, flexible TRM membranes engineered with precise lateral dimensions function as discrete “microwave-absorbing leaves,” where electromagnetic wave propagation is modulated via two-dimensional mesoscale structural features to enable accurate and programmable wave control.

Nano Research
Open Access
Research Article

2D TiN/graphene metacomposite for photosynthesis-inspired EM modulation and multi-stage attenuation

Yi Zhang, Lu Zhang, Menghan Zhang, Yaqin Ding, Kailin Feng, Lei Zhang, Cuiping Li, Chunhong Gong ✉

National & Local Joint Engineering Research Center for Applied Technology of Hybrid Nanomaterials, College of Chemistry and Molecular Sciences, Henan University, Kaifeng 475004, China

Received: 5 August 2026 **Revised:** 17 August 2026; **Accepted:** 22 August 2026

✉ Address correspondence to gong@henu.edu.cn

Cite this article: *Nano Research*, 2026, 19, 94909140 https://doi.org/10.26599/NR.2026.94909140

ABSTRACT: Metacomposites offer a transformative approach to simultaneously optimize impedance matching and dielectric loss in microwave absorption materials (MAMs), especially under thermal fluctuations. Inspired by broadleaf foliage, we design sub-wavelength regime flexible TiN/reduced graphene oxide (RGO) membranes (TRMs) as “microwave-absorbing leaves”. A critical geometric threshold emerges from the ratio of membrane lateral size (L) to incident wavelength (λ_m). When $L/\lambda_m < 0.1$, minimal interfacial reflection enables efficient wave transmission. At $L/\lambda_m \approx 0.1$, TRMs trigger multi-scattering and cascaded attenuation, which boosting dielectric loss while maintaining near-unity impedance matching. In contrast, when $L/\lambda_m > 0.1$, electromagnetic waves are reflected at the macroscopic interface, resulting in severe impedance mismatch, poor wave penetration, and markedly reduced absorption. Leveraging this sub-wavelength scale control, optimized TRMs-2 achieves an outstanding minimum reflection loss (RL_{min}) of −57 dB at only 1.1 wt.% filler loading and a broad effective bandwidth of 3.8 GHz. It also exhibits robust thermal stability from 298 to 573 K. This work establishes a clear link between two-dimensional (2D) mesoscale geometry and electromagnetic dissipation, providing a biomimetic paradigm for lightweight, thermally stable MAMs that break the traditional trade-off between impedance matching and attenuation.

KEYWORDS: titanium nitride; metacomposite; biomimetic; electromagnetic dissipation mechanism; microwave absorption material

1 Introduction

The proliferation of high-throughput wireless technologies and advanced electronics has intensified electromagnetic interference and radiation pollution, necessitating high-performance microwave absorption materials capable of operating in complex, thermally dynamic environments [1-3]. The efficacy of such materials hinges on the delicate synergy between impedance matching and dielectric loss [4, 5]. However, conventional composites often suffer from “temperature drift,” wherein thermally activated charge carrier migration disrupts this synergy, leading to unstable absorption performance at elevated temperatures [6, 7]. This thermally induced decoupling of impedance and attenuation characteristics remains a fundamental bottleneck hindering practical applications [8, 9].

Titanium nitride (TiN), a refractory ceramic with metallic conductivity, has emerged as a prime candidate for thermally stable absorbers owing to its exceptional thermal stability and corrosion resistance [10]. While current strategies predominantly focus on morphological engineering and heterostructure design to boost intrinsic loss, they largely neglect the critical role of sub-wavelength scale architecture in governing the electromagnetic response [11, 12]. Addressing this gap requires a paradigm shift from merely tuning intrinsic properties to architecting structural geometries that actively regulate wave-matter interactions [13, 14].

Metacomposites represent an emerging class of materials that synergistically integrate materials science with periodic/aperiodic structural design. By engineering dielectric materials into sub-wavelength functional units, their discrete arrangement enhances anti-reflection effects and provides substantial intrinsic loss capabilities, thereby achieving the decoupling of strong attenuation from impedance matching. Furthermore, metacomposites facilitate controlled reflection and scattering of EMWs by meticulously engineering the conductivity, size, and spatial configuration of the functional units, offering a pioneering approach to further enhance microwave absorption efficiency [15]. Pioneering research has shown that discretely distributing mesoscopic functional units suppresses macroscopic conductive networks, alleviating temperature-related fluctuations while amplifying the electromagnetic responsiveness of microwave absorbing units. This approach not only boosts the overall attenuation capacity but also provides a feasible structural paradigm for maintaining dielectric stability in MAMs across a broad temperature spectrum [16]. Nevertheless, the realization of precise electromagnetic wave modulation and maximum attenuation still poses a major challenge [17, 18].

Bioinspiration offers a compelling route for advancing functional material design [19-21]. As illustrated in Fig. 1(a), after thousands of years of natural selection, broad-leaved plants have evolved complex planar structures in their leaves, which exhibit remarkable optical properties that are different from those of coniferous trees. These multilayer leaf systems optimize light penetration while maximizing photosynthetic surface area and light-harvesting efficiency through reflection and scattering [22]. This natural design provides a promising strategy for maximizing energy conversion efficiency by enhancing the electromagnetic response of absorbing units and optimizing wave-matter interactions [23] The discrete layers enhance incident EMW transmission across the surface. Upon entry, waves undergo multiple scattering, reflection, and repeated in-plane and interlayer re-transmission, creating a dense propagation pathway that maximizes electromagnetic energy dissipation [24, 25]. Furthermore, the intrinsic planarity of 2D units enables precise control over their orientation and spatial distribution, thereby enabling effective control over wave dynamics within a lightweight architectur [26].

Consequently, it overcomes the long-standing limitations of conventional absorbers in balancing structural complexity and effective loss mechanisms [27]. The key point is that, according to the theory of EMW propagation in dielectric media, the relative relationship between the unit size (L) and the wavelength of EMWs within the composites (λ_m) fundamentally determines the propagation mode of EMWs [28]. When L/λ_m<0.1, the unit lies in the electrically small regime, where EMWs penetrate the entire structure almost unimpeded. Energy dissipation in this regime relies primarily on intrinsic dielectric loss, manifesting as a deep-penetration volumetric dissipation mode. When L/λ_m≈0.1, the absorbing unit begins to be recognized by the EMW and starts to exhibit sub-wavelength resonant behavior. Consequently, the loss mode shifts from "volumetric dissipation governed by intrinsic material properties" to "localized dissipation via resonant coupling of discrete structural units." In this regime, the unit no longer merely polarizes passively under the external electromagnetic field; instead, it begins to interact strongly with the EMW as an independent resonant dipole. This strong interaction causes EMWs to undergo multiple reflections and scattering between layers, further amplifying the electromagnetic response [29]. When L/λ_m>0.1, strong surface waves and resonance effects confine the incident waves to the material surface, forming a surface-confined mode, where most of the energy is reflected rather than absorbed[30]. This electrical-size-driven mode evolution enables programmable modulation of wave–matter interactions through lateral size engineering, offering significant potential for on-demand customization of absorption performance.

Herein, we present a bioinspired metacomposite featuring sub-wavelength scale flexible TiN/RGO membranes as "microwave-absorbing leaves." By integrating high intrinsic loss with precise lateral size engineering, we establish a clear structure-property relationship where sub-wavelength scale geometry dictates electromagnetic dissipation. Systematic investigations demonstrate that, at the same filler content (1.1 wt.%), the absorption peak gradually shifts toward lower frequencies as the TRMs unit size increases. When L/λ_m≈0.1, TRMs-2 exhibits a distinct absorption peak at 10 GHz, delivering a minimum reflection loss (RL_{min}) of −57 dB with an effective absorption bandwidth (EAB) of 3.8 GHz. Furthermore, the discrete distribution of TRMs units ensures stable impedance matching across the temperature range of 298 to 573 K, exhibiting exceptional thermal stability. This study not only elucidates the dimensional threshold governing wave-matter interactions in metacomposites but also provides a biomimetic paradigm for breaking the traditional trade-off between impedance matching and attenuation in lightweight, temperature-invariant microwave absorption materials.

2 Experimental

2.1 Materials

Graphene oxide (GO) was synthesized via the Hummers' method. Tetrabutyl titanate ($Ti(OC_4H_9)_4$, TBT), polyvinylpyrrolidone (PVP), and zirconium acetate ($Zr(OAc)_4$) were obtained from Aladdin Reagent (Shanghai) Co., Ltd. Acetic acid and polydimethylsiloxane (PDMS) were purchased from Luoyang Haohua Chemical Reagent Co., Ltd. and Dow Corning, respectively.

2.2 Preparation of TiN/RGO membranes (TRMs)

First, 8 g of anhydrous ethanol, 4 g of glacial acetic acid, and 1 g of polyvinylpyrrolidone (PVP) were added into a 25 mL conical flask and stirred until completely dissolved. Subsequently, a certain amount of tetrabutyl titanate (TBT) and zirconium acetate ($Zr(OAc)_4$) (with a Ti-to-Zr molar ratio of 4:1) were introduced, and the mixture was continuously stirred until a homogeneous spinning solution with appropriate viscosity was obtained. The spinning solution was then drawn into a syringe equipped with a custom designed needle and subjected to electrospinning, with aluminum foil used as the collector. The as-spun fibrous membrane was dried and subsequently calcined at 500℃ for 2 h at a heating rate of 2 ℃/min to obtain TiO_2/ZrO_2 composite fiber membranes. Thereafter, the membrane was immersed in a cetyltrimethylammonium bromide (CTAB) solution at a concentration of 0.1 g/mL, and the CTAB-modified fiber membrane was obtained after drying. Through vacuum-assisted filtration, a graphene oxide dispersion (1 mg/mL) was uniformly deposited onto the membrane. Finally, the membrane was calcined at 900 ℃ under an NH_3 atmosphere to obtain the TiN/RGO membranes (TRMs). The resulting TRMs had a thickness of 0.38 mm, and the RGO content accounted for 4.8 wt.% of the total mass of the fibrous membrane.

2.3 Preparation of TRMs/PDMS metacomposites

TRMs were impregnated with a PDMS/KH550 mixture and cured at 80℃ for 3 h. The resulting material was cut into slices of varying dimensions (1 mm × 1 mm, 2 mm × 2 mm, and 3 mm × 3 mm). These sheets were then placed in a PTFE mold (22.86 mm × 10.16 mm × 2.5 mm) within a PDMS matrix and arranged in parallel layers (6 layers in total), where the TRMs weighed 0.0074 g and the PDMS weighed 0.673 g. After curing at 80 °C for 3 h, TRMs/PDMS metacomposites with a filler content of 1.1 wt.% were obtained. The samples were labeled as TRMs-1, TRMs-2, and TRMs-3 according to the sheet size. Furthermore, in order to highlight the advantage of the 2D unit design, an equivalent mass of TRMs fiber membrane was ground into powder and uniformly mixed with silicone rubber to prepare a control sample, designated as TRMs-0.

2.4 Characterization

Crystal structure and phase composition were analyzed using X-ray diffraction (XRD, Bruker D8 Advance, Cu-Kα radiation, λ = 1.5406 Å) and confocal Raman spectroscopy (Renishaw RM-1000, 532 nm laser excitation). Surface morphology and elemental distribution were examined by scanning electron microscopy (SEM, Gemini 500) coupled with energy-dispersive spectroscopy (EDS). The electrical conductivity of the composite fiber membranes was measured using a four-point probe resistivity meter (RTS-8). Electromagnetic parameters were measured using a vector network analyzer (Ceyear 3672B-S, China Electronics Technology Group Corporation) in a sealed heating chamber over a frequency range of 8.2-12.4 GHz and a temperature range of 298–573 K under an argon atmosphere. The measurements were conducted with a heating rate of 4℃/min, and the temperature was held for 5 min at every 20℃ interval, and the data were recorded at each stabilized temperature.

3 Results and discussion

3.1 Custom-tailored design and electromagnetic simulation of TRMs

The inherent brittleness of ceramic fibers presents a major obstacle to the controllable design of advanced composites. To overcome this limitation, we first fabricated precursor nanofibers via electrospinning (Fig. 1(b)) and then removed polyvinylpyrrolidone (PVP) through high-temperature treatment to obtain a TiO_2/ZrO_2 nanofibrous membrane [10]. Leveraging the electrostatic interaction between cetyltrimethylammonium bromide (CTAB) and graphene oxide, GO nanosheets were uniformly dispersed throughout the TiO_2/ZrO_2 fiber matrix. Subsequent in-situ thermal nitridation transformed the network into a TRMs. The RGO component not only fills the inter-fiber voids but also establishes enhanced electrical connectivity across the network [31]. Crucially, the distinct electrical properties of the constituent phases induce abundant heterointerfaces [32]. These interfaces facilitate pronounced interfacial polarization, serving as a pivotal mechanism for boosting microwave absorption.

Fig. 1(c) displays the microstructure and morphology of the synthesized TRMs. The TiN/ZrO_2 fibers (blue regions) interconnect to form vein-like structures reminiscent of plant leaves, providing mechanical support and charge transport pathways that ensure efficient carrier migration during the electromagnetic response. Reduced graphene oxide (RGO) nanosheets (purple regions) are uniformly distributed on the TiN fiber membranes, further strengthening the TiN/ZrO_2 fiber network structure. They mimic the leaf mesophyll, acting as the EMWs-harvesting units and capture incident EMWs by leveraging their intrinsic dielectric loss capabilities [33]. Furthermore, the multi-layer arrangement of 2D absorbing units in the metacomposite facilitates the transmission of EMWs between unit layers, accompanied by multiple scattering and reflection, thereby maximizing the dissipation efficiency of electromagnetic energy [34]. The crystal structure and phase composition of the TRMs was systematically characterized by XRD and Raman spectroscopy. As shown in Fig. 1(d), the XRD pattern displays distinct diffraction peaks at 36.8°, 42.8°, 62.1°, 74.4°, and 78.3°, corresponding to the (111), (200), (220), (311), and (222) planes of the face-centered cubic TiN phase (PDF#38-1420). Peaks at 30.5°, 34.6°, 35.6°, 50.5°, 59.3°, and 60.5° match the (101), (002), (110), (112), (103), and (211) planes of the tetragonal ZrO_2 phase (PDF#88-1007), confirming the coexistence of TiN and ZrO_2 in the composite. Additionally, a broad diffraction peak at 24°-28° is attributed to RGO, further verifying the successful synthesis of the multiphase material. Raman spectroscopy (Fig. 1(e)) provides insight into the chemical bonding states. Peaks at 151 cm^{-1}, 249 cm^{-1}, 413 cm^{-1}, and 610 cm^{-1} are characteristic of TiN, while the absence of distinct ZrO_2 peaks is likely attributed to its weak Raman scattering sensitivity. Notably, two clear peaks near 1350 cm^{-1} (D band, defect-induced) and 1580 cm^{-1} (G band, graphitic carbon) confirm the successful incorporation of RGO into the TRMs. Elemental mapping (Fig. 1(f)) further confirms the uniform distribution of Ti, N, Zr, O, and C across the TRMs, verifying the successful integration of both TiN and ZrO_2 phases. The abundant heterogeneous interfaces formed within the TRMs play a critical role in enhancing polarization dissipation, a key requirement for microwave-absorption applications [35, 36]. These combined results unambiguously demonstrate the successful synthesis of the TRMs with a well-defined multiphase structure.

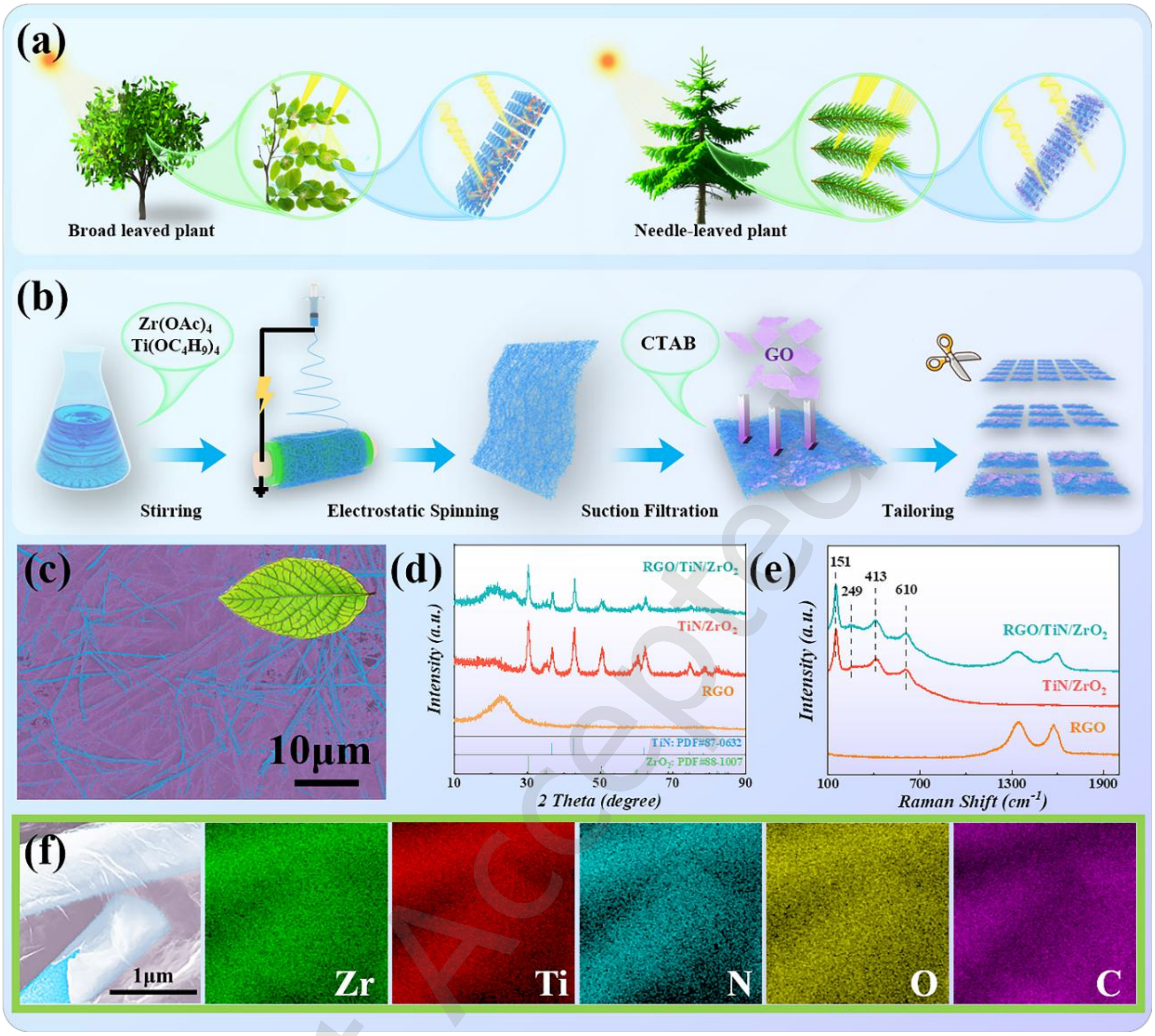

Fig. 1 (a) Schematic illustration of the light-harvesting mechanism in nature, comparing broad-leaved and needle-leaved plants. (b) Schematic diagram illustrating the fabrication process of the TRMs/PDMS metacomposite; (c) SEM image of the TRMs; (d) XRD pattern and (e) Raman spectrum of the TRMs, along with (f) their corresponding elemental mapping images.

To identify the optimal dimensional threshold for synchronizing impedance matching with attenuation, we calculated the unit size of the 2D TiN/RGO units relative to the wavelength within the silicone rubber matrix (see Text S1 in the Electronic Supplementary Material). Across the 8.2-12.4 GHz range, the intra-medium wavelength (λ_m) decreases from 22.11 mm to 14.66 mm. Notably, a unit dimension of 2 mm approximates $\lambda_m/10$ at the target frequency (~10 GHz), a critical threshold demarcating the transition from the electrically small regime to the sub-wavelength regime. At this scale ($L/\lambda_m\approx0.1$), the structure is poised to minimize interface reflection while maximizing the density of optical states for internal multi-scattering [30]. Consequently, 2 mm was selected as the representative intermediate dimension to systematically probe the evolution from sub-wavelength resonance to geometric scattering.

Table 1. The free-space wavelength and the wavelength within the composite material corresponding to the X-band.

Frequency (GHz)	λ_0 (mm)	ε_r	λ_m (mm)	λ_m/10(mm)
8.20	36.60	2.73	22.11	2.21
10.00	30.00	2.78	17.97	1.79
12.40	24.20	2.72	14.66	1.46

λ_0 represents the free-space wavelength, and λ_m represents the wavelength of electromagnetic waves within the composites.

Electromagnetic simulations enable the visualization of field distributions and dynamic electromagnetic responses in composite materials, offering novel insights into structure-performance relationships. As illustrated in Fig. S2, three models different scales were constructed in CST to analyze the electric field intensity (|E|) distribution and power loss density (P) at 10 GHz. This approach aims to elucidate the electromagnetic response mechanism of the TRMs absorber and thereby guides more efficient and optimized design of microwave absorbers. Here, the |E| distribution reflects microwave propagation within the system, while the P distribution indicates the attenuation of incident waves. The results demonstrate a clear correlation between functional-unit size and electromagnetic response (Fig. 2(a-c)). When the unit size is 1 mm (TRMs-1), the functional units effectively suppress the conductivity of the TRMs. This leads to pronounced |E| and P distributions within the TRMs-1 structure, indicating that electromagnetic waves (EMWs) penetrate the material with minimal reflection. The uniform field distribution confirms excellent impedance matching between TRMs-1 and the incident wave. As the unit size increases to 2 mm (TRMs-2), the |E| distribution gradually weakens, and the P distribution becomes inhomogeneous, concentrating near the edges of the functional units. This suggests that larger units enhance reflection at unit boundaries, creating multiple reflections and scattering interfaces. These interfaces promote interlayer resonance and cancellation effects, thereby accelerating EMW attenuation [37]. When the unit size is further increased to 3 mm (TRMs-3), both |E| and P are predominantly confined to the material surface. This indicates that a larger proportion of the incident wave is reflected rather than dissipated within the material. This behavior can be attributed to the larger unit size inside TRMs-3, which, under EMW excitation, induces longer-range charge migration. The resulting periodic oscillations form localized micro-currents that reflect the EMWs, thereby reducing effective microwave penetration and limiting energy transfer into the material [38]. In summary, the simulation results not only validate the feasibility of geometry-driven impedance modulation for tuning absorption, but also establish a quantitative relationship between unit size and electromagnetic performance, thereby defining the optimal size range for TRMs to balance impedance matching and scattering loss. This provides valuable guidance for engineering high-performance microwave absorbers with tailored functionalities.

Based on equivalent- circuit theory, the relationship between the absorbing performance of the composite material and its unit size was further analyzed [39]. As shown in Fig. 2(d), the interaction between a functional unit and its neighbors is equivalently represented as series or parallel inductive elements on a transmission line. Under perpendicular electromagnetic incidence, the interval between functional units perpendicular to the electric- field excitation plane can be treated as a capacitance (C), while the unit itself perpendicular to the magnetic- field excitation plane acts as an inductance (L)[40]. The resonant frequency f_0 of the parallel LC circuit is given by:

$$C = \frac{\varepsilon S}{4\pi k d} \quad (1)$$

$$f_0 = \frac{1}{2\pi\sqrt{LC}} \quad (2)$$

Where S is the plate area, f_0 the resonant frequency, ε the permittivity, d the plate spacing, and k the electrostatic force constant. Equations (1) and (2) show that the capacitance C increases with unit size due to the enlargement of S, leading to a decrease in f_0. As seen in Fig. 2(e), the frequency corresponding to the RL_{min} shifts toward lower frequencies as the TRMs unit size grows, exhibiting a clear size effect.

The electromagnetic response and absorption performance of TRMs/PDMS metacomposites at different scales were further examined through their electromagnetic parameters. Reflection loss is calculated as follows [16]:

$$RL = 20\,log\left|\frac{Z_{in}-Z_0}{Z_{in}+Z_0}\right| \quad (3)$$

$$Z_{in} = Z_0\sqrt{\mu_r / \varepsilon_r}\,tanh\left[j(2\pi f d / c)\sqrt{\mu_r\varepsilon_r}\right] \quad (4)$$

Here, Z_{in} and Z_0 denote the input impedance of the absorber and the impedance of free space, respectively. The equivalent wave impedance depends on the complex permittivity ε_r and permeability μ_r, while f, d, and c represent microwave frequency, absorber thickness, and the speed of light. The RL value directly reflects absorption performance, with RL < -10 dB typically defining the effective absorption bandwidth (EAB), indicating over 90% microwave attenuation.As shown in Fig. 2(f-h), TRMs- 1 possesses small discrete internal units, resulting in insufficient loss capability to meet practical absorption requirements. In contrast, TRMs-2, with optimized geometric dimensions, demonstrates excellent microwave absorption: it achieves a strong absorption peak of -57 dB near 10 GHz and an EAB of 3.8 GHz at a matching thickness of 2.5 mm, making it a promising candidate for high-performance absorption applications. However, when the unit size increases to 3 mm (TRMs-3), a larger localized conductive network forms within the material. Under electromagnetic excitation, the sinusoidal alternating electric field induces periodic oscillations of charges in the film, generating surface-alternating microcurrents that impede efficient wave propagation rather than enhancing absorption [41]. This results in a marked deterioration of performance for TRMs-3, where the RL_{min} drops to -14 dB and the EAB contracts to just 0.8 GHz, failing to meet the criteria for practical deployment. As a control, an equivalent mass of TRMs fiber membrane was ground into powder and uniformly dispersed in silicone rubber to fabricate reference sample TRMs-0. As shown in Fig. S3, although the powder is uniformly dispersed, TRMs-0 exhibits a lower imaginary permittivity ε_r'', smaller attenuation constant (α), and its $|Z_{in}/Z_0|$ is further away from 1. This direct comparison quantitatively confirms the structural advantage of the bioinspired architecture and clearly shows that the exceptional performance of TRMs-2 originates from its unique leaf-like morphology rather than merely the material composition.

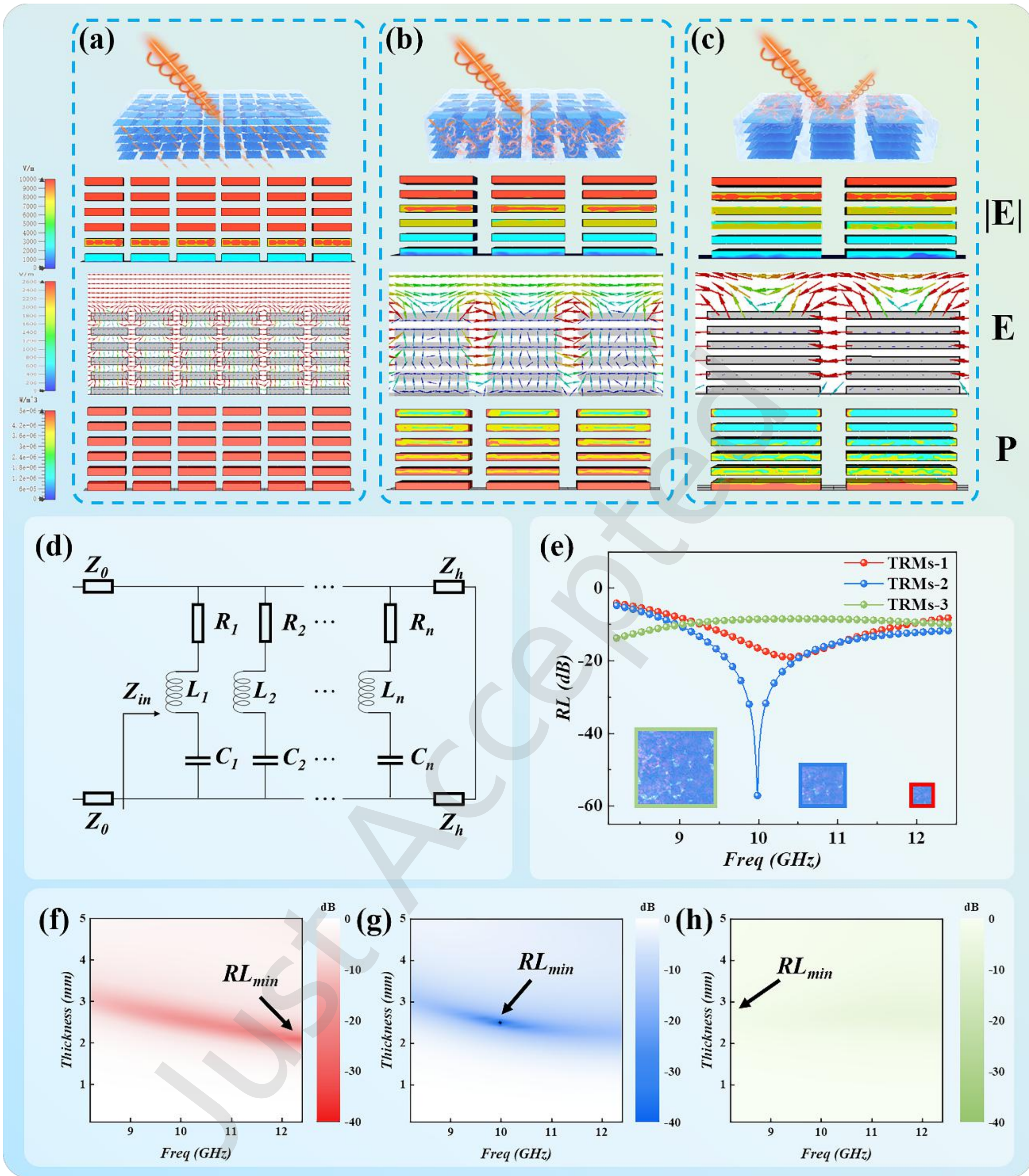

Fig. 2 Electric field and power loss density of (a) TRMs-1, (b) TRMs-2, and (c) TRMs-3 at 10.0 GHz, respectively. (d) Equivalent circuit model of the TRMs/PDMS metacomposites. (e) Microwave absorption performance at 2.5 mm thickness. Microwave absorption properties of (f) TRMs-1, (g) TRMs-2, and (h) TRMs-3.

3.2 The Wide Temperature Range Absorption Performance and Attenuation Mechanism for TRMs/PDMS metacomposites

Previous studies have demonstrated that subwavelength-scale units discretely distributed within microwave absorption materials can effectively decouple impedance matching and attenuation capability across a broad temperature range [17]. Fig. 3(a-f) presents the frequency-dependent microwave absorption performance of the metacomposites at a fixed thickness of 2.3 mm over the temperature interval of 298 K to 573 K. The results reveal distinct temperature-dependent behaviors: while the absorption of TRMs-1 gradually degrades with rising temperature, TRMs-2 maintains its reflection loss below -10 dB throughout the entire range, demonstrating exceptional thermal stability. Notably, TRMs-3 exhibits relatively weak absorption at room temperature, yet its performance paradoxically strengthens as the temperature increases.

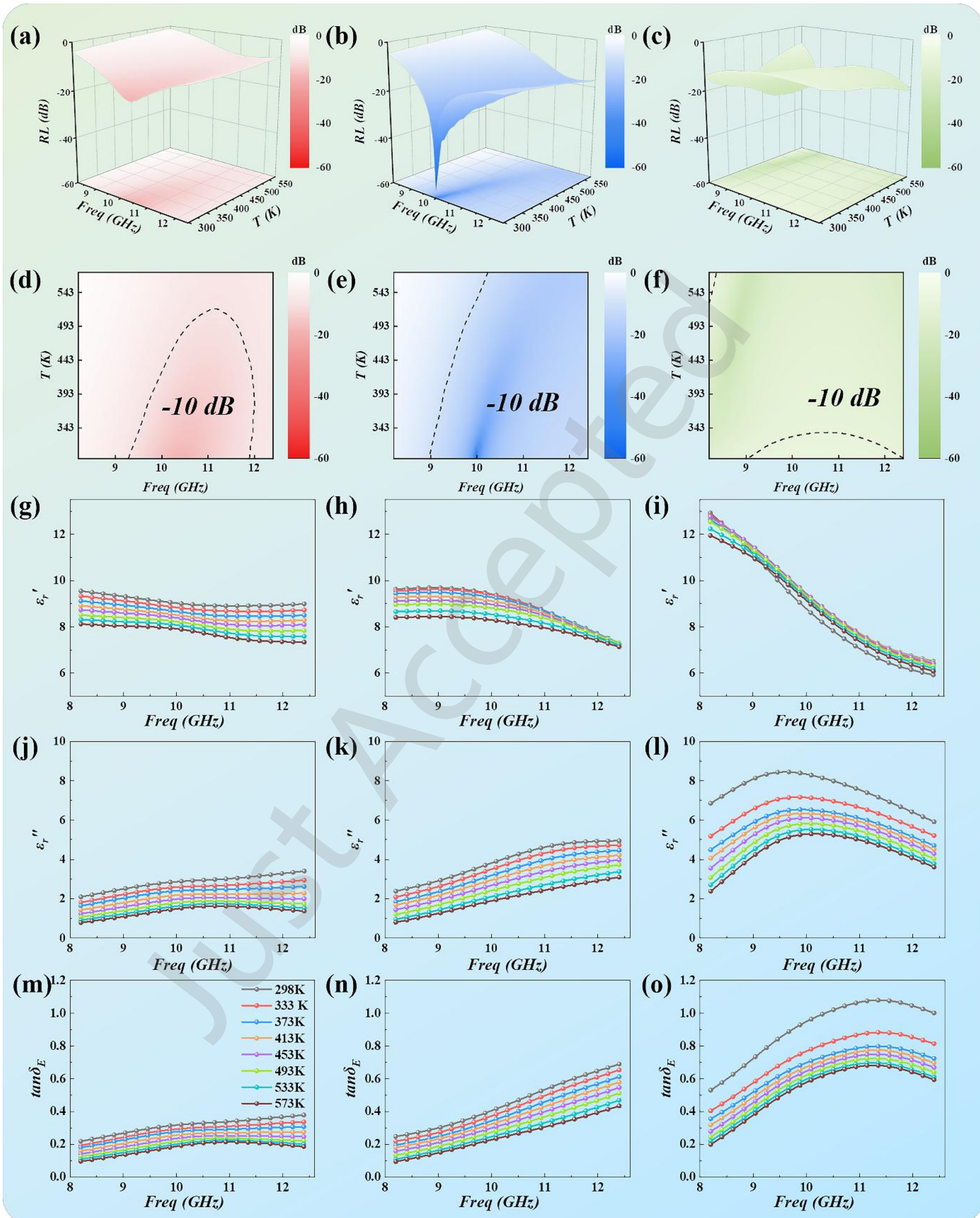

Fig. 3 Calculated microwave absorption properties: (a-c) 3D RL plots and (d-f) corresponding 2D contour maps of TRMs-1, TRMs-2, and TRMs-3 (2.3 mm thickness, 298-573 K). Temperature-dependent dielectric properties (ε_r', ε_r'' and, $tan\,\delta_E$) of (g, j, m) TRMs-1, (h, k, n) TRMs-2, and (i, l, o) TRMs-3.

To elucidate the electromagnetic response of TRMs absorbing units over a wide temperature span, the electromagnetic parameters of TRMs/PDMS metacomposites were analyzed from 298-573 K. Dielectric absorbing materials primarily dissipate microwave energy through conductive and polarization losses. Conductive loss arises from the excitation of charge carriers, which convert electrical energy into heat. Polarization loss originates from polarization and relaxation effects caused by imbalanced electric field energy under high-frequency electromagnetic excitation [42]. As shown in Fig. 3(g-i), the real part of permittivity ($\varepsilon_r^{'}$) of the TRMs/PDMS metacomposites displays pronounced dispersion, a phenomenon attributed to the distinct frequency responses of various polarization mechanisms (electronic, ionic, and dipolar) within the material [43]. Notably, the dispersion intensity increases gradually with TRMs unit size, underscoring the crucial role of unit scale in modulating dielectric dispersion. Correspondingly, as can be observed from Fig. 3(j-o), both the imaginary part of the complex permittivity ($\varepsilon_r^{''}$) and the dielectric loss tangent ($tan\,\delta_E$) of the metacomposite gradually increase with the growing unit size. This trend is primarily attributed to the enhanced charge energy excited by the electromagnetic field as the unit size increases, which intensifies the interfacial polarization effect [44]. Specifically, the enlarged lateral dimensions extend the charge migration distance within the conductive network, promoting the accumulation of space charges at abundant heterointerfaces and significantly enhancing the interfacial polarization intensity [45]. Meanwhile, in the discretely distributed unit system, long-range charge migration is suppressed; the accumulated charges cannot be instantaneously released during alternating field reversal, but are instead dissipated through a relaxation process, manifesting as enhanced polarization relaxation [46]. Consequently, it exhibits enhanced EMW dissipation capabilities.

To elucidate the electromagnetic attenuation mechanism of the TRMs absorbing units, we employed the Debye model to describe their relaxation processes, as represented by Equation (5-7) [7]:

$$\varepsilon_r^{'} = \varepsilon_\infty + \frac{\varepsilon_s - \varepsilon_\infty}{1+\omega^2\tau^2} \quad (5)$$

$$\varepsilon_r^{''} = \frac{(\varepsilon_s - \varepsilon_\infty)\omega\tau}{1+\omega^2\tau^2} \quad (6)$$

$$\left(\varepsilon_r^{'} - \varepsilon_\infty\right)^2 + \varepsilon_r^{''2} = \varepsilon_s - \varepsilon_\infty \quad (7)$$

Where ω is the angular frequency, ε_∞ and ε_s the optical and static dielectric constants, respectively, τ the relaxation time. Cole-Cole plots are widely used to identify Debye-type relaxation processes in materials, where each distinct semicircle corresponds to an individual Debye relaxation mechanism. As shown in Fig. 4(a), the Cole-Cole curves of TRMs-2 and TRMs-3 exhibit smooth, well-defined semicircular arcs without trailing segments. This characteristic contrasts with the distorted arcs observed in TRMs-1, indicating that increasing the unit dimensions of the TRMs enhances charge transport within the localized conductive network. Such enhancement modifies the dielectric properties of the functional units and intensifies the polarization relaxation behavior. Furthermore, the transmission, multiple reflections, and scattering of EMWs within the TRMs/PDMS metacomposites create more complex propagation pathways. These effects strengthen the interactions between the waves and the abundant heterogeneous interfaces in the TRMs, further promoting polarization loss capabilities [36].

To quantitatively evaluate the influence of TRMs unit size on conductive and polarization losses, we performed fitting calculations using Equation (8) by rewriting the Debye relaxation model into a circular equation form.

$$\varepsilon_r^{''}(\omega) = \varepsilon_p^{''} + \varepsilon_c^{''} = (\varepsilon_s - \varepsilon_\infty)\frac{\omega\tau}{1+\omega^2\tau^2} + \frac{\sigma}{\varepsilon_0\omega} \quad (8)$$

Where σ the electrical conductivity, ε_0 the permittivity of free space, $\varepsilon_p^{''}$ the contribution from polarization relaxation, and $\varepsilon_c^{''}$ the conduction-related loss. The equivalent electrical conductivity (σ) of the TRMs/PDMS metacomposites, derived from fitting calculations based on Equations (8), exhibits a gradual increase with expanding unit dimensions (Fig. 4(b)). To further decouple the contributions of conductive loss $\varepsilon_c^{''}$ and polarization loss $\varepsilon_p^{''}$ to the overall dielectric loss, we compared their respective magnitudes across the X-band (Fig. 4(c-f)). The results demonstrate that polarization loss dominates over conductive loss throughout the entire frequency range. This predominance arises from the 2D discrete distribution of TRMs units, which effectively suppresses long-range charge migration by isolating conductive networks within individual units. This configuration induces a “sub-percolation state”, where conductive pathways remain localized rather than interconnected across the material. Consequently, conductive loss is significantly weakened, while polarization loss, enabled by abundant heterogeneous interfaces becomes the primary dissipation mechanism.

The temperature-dependent dielectric behavior further corroborates this loss dominance. As shown in Fig. S4, the observed decrease in complex permittivity (both $\varepsilon_r^{'}$ and $\varepsilon_r^{''}$) with increasing temperature can be attributed to two synergistic mechanisms governing the dielectric behavior of the metacomposites. First, the TRMs units are individually encapsulated within the matrix, preventing the formation of continuous conductive pathways. This design limits long-range electron transport, thereby restraining conductive loss. With rising temperature, thermally induced electron scattering further inhibits carrier mobility and lowers the overall conductivity. Second, elevated temperature intensifies the thermal agitation of dipoles, increasing the degree of orientational disorder. Although thermal motion lowers the energy barrier for dipole reorientation, the enhanced thermal disorder significantly impedes effective dipole alignment under the alternating electric field, thereby weakening the polarization relaxation strength [47]. Consequently, the polarization loss capability gradually diminishes with increasing temperature, manifested as a decrease in $\varepsilon_r^{''}$. Concurrently, elevated dipole disorder weakens the local electric field response of the system, manifesting as a macroscopic reduction in $\varepsilon_r^{'}$.

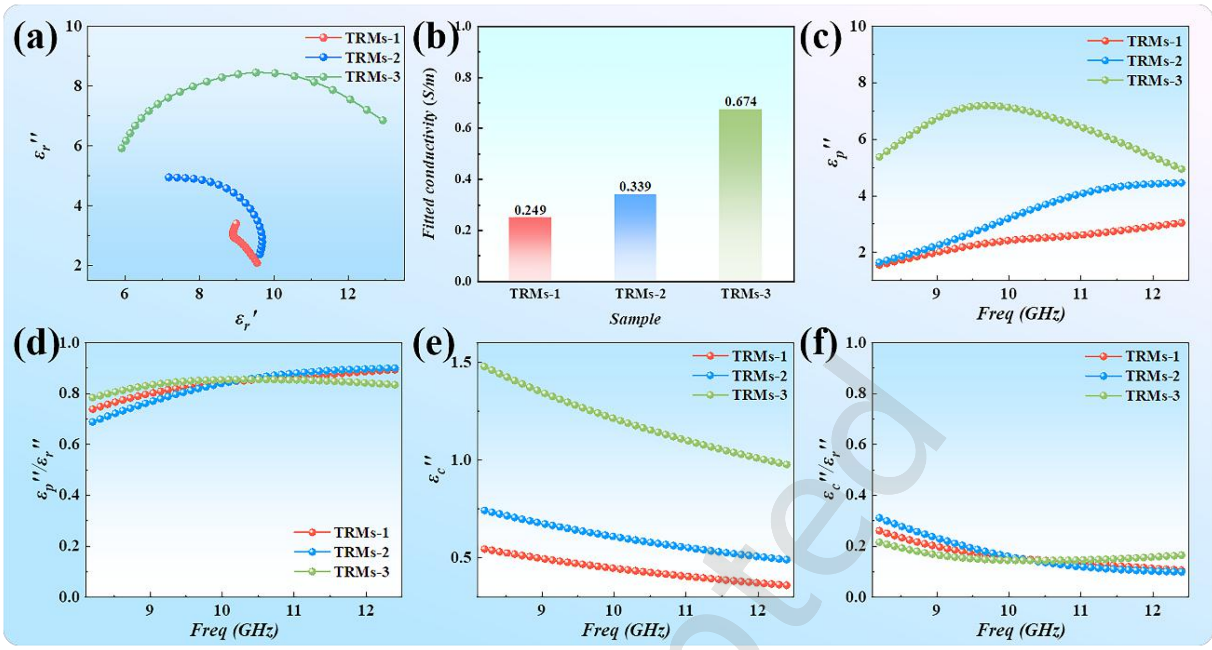

Fig. 4 (a) Cole-Cole plots and (b) equivalent electrical conductivity of the TRMs/PDMS metacomposites. Conduction and polarization losses in TRMs/PDMS metacomposites: (c) fitted conduction loss and (d) fitted polarization loss as functions of frequency. (e) Proportion of conduction loss and (f) proportion of polarization loss.

Attenuation capacity and impedance matching are two decisive factors governing the performance of microwave absorbing materials (MAMs). As shown in Fig. 5(a–c), the attenuation constant (α) of the TRMs/PDMS composites exhibits a pronounced size-dependent enhancement, which is driven by two synergistic mechanisms: first, the abundant heterogeneous interfaces coordinately promote strong interfacial polarization; second, multiple scattering events within the fibrous architecture trap EMWs and prolong the wave–matter interaction duration [48]. Notably, the decrease in α with increasing temperature further

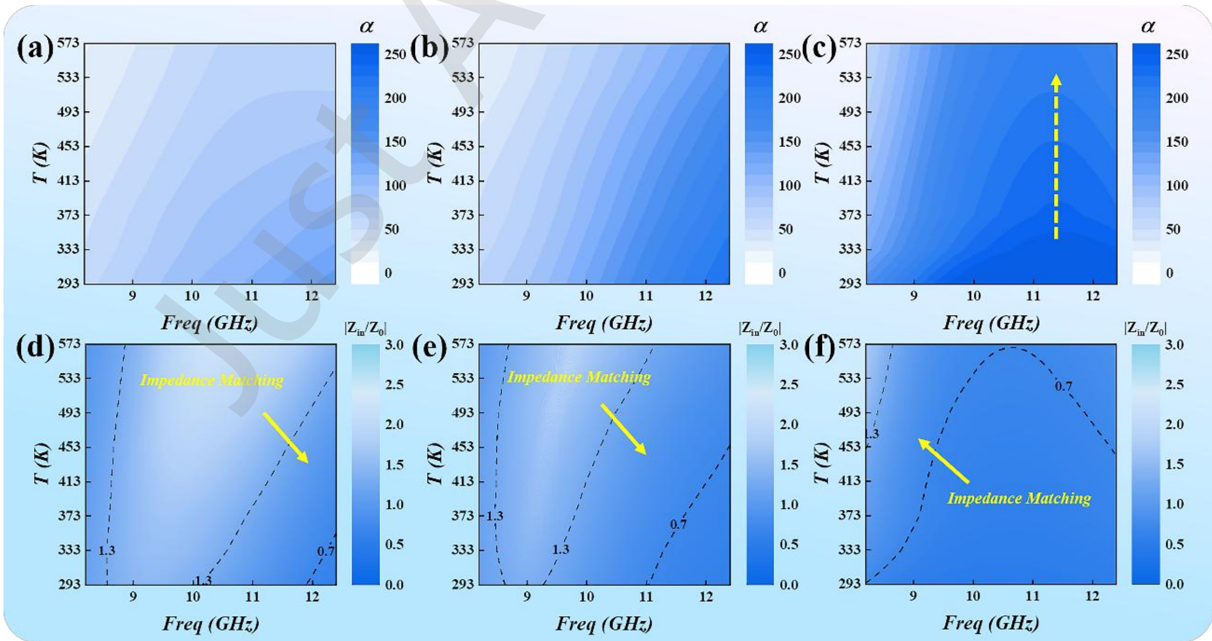

confirms that polarization loss dominates over conduction loss in this system.

Fig. 5 (a-c) Attenuation constant (α) and (d-f) normalized input impedance magnitude $|Z_{in}/Z_0|$ of the TRMs/PDMS metacomposites as a function of frequency at a fixed thickness of 2.3 mm, measured across temperatures from 298 -573 K.

Optimal absorption performance requires a delicate balance between $|Z_{\mathrm{in}}/Z_0|$ and α. While a high α favors energy dissipation, ensuring effective wave penetration and minimizing reflection hinges on bringing $|Z_{\mathrm{in}}/Z_0|$ as close to unity as possible. Specifically, smaller unit sizes facilitate deeper penetration of EMWs into the material, maximizing energy consumption through thorough interactions with internal interfaces. Conversely, excessively large units generate stronger alternating microcurrents at the membrane interfaces, impeding wave propagation and deteriorating impedance matching, as illustrated in Fig. 5(d-f) [49]. Among them, TRMs‐2 achieves a synergistic integration of multiple attenuation mechanisms while maintaining superior impedance matching, confirming its superior attenuation potential at this optimized scale. Moreover, the discrete conductive networks designed in this architecture endow unique anti-reflection characteristics. Critically, these networks exhibit temperature-insensitive electromagnetic properties over a wide thermal range (298-573 K), ensuring consistent absorption performance even under temperature fluctuations.

As summarized in Table 2, recent studies on TiN-based composites report a range of EMW absorption performance [50-57]. In contrast, the 2D absorbing units (TRMs) developed in this work achieve exceptional attenuation efficiency at an ultralow filler loading of 1.1 wt.%, as evidenced by systematic comparative analysis. This superior performance originates from a rational structural design that strategically redirects EMW propagation paths while synergistically utilizing intrinsic loss mechanisms, thereby substantially enhancing wave-material interactions. Notably, these TRMs-based absorbers also meet lightweight requirements without sacrificing absorption efficiency, outperforming conventional high-loading ceramic-based absorbers documented in earlier studies.

Table 2 Ceramic composites for electromagnetic wave absorption reported in recent literature.

Samples	Filler content (wt. %)	EAB (<-10 dB)	RL_{min} (298K)	RL_{min} (573K)	Ref.
TiN/paraffin	20	2.1	– 46.7	-	[50]
NbTiN/paraffin	20	0.8	-44.97	-	[51]
SiCN(Fe)/Al_2O_3	-	4	-18	-	[52]
GR-TiN/PLA/TPU	4	5	-29.08	-	[53]
SiC/SiCN	-	4.2	-18.56	-17.5	[54]
TiN/Al_2O_3	10	2.18	-37.82	-	[55]
CMO-PSAE	50	4.16	-53.01	-	[56]
TiN/paraffin	20	1.5	-45.8	-	[57]
TRMs/PDMS	1.1	3.8	-57	-18	This work

3.3 Radar cross-section simulation of TRMs/PDMS metacomposites

The radar cross-section (RCS), a key parameter in stealth technology, quantifies the intensity of radar echoes from a material under illumination, reflecting the practical performance of electromagnetic wave-absorbing materials under far-field conditions [58]. In this study, CST Studio software was used to simulate a Perfect Electric Conductor (PEC) plate measuring 180 mm × 180 mm × 0.5 mm. The RCS reduction was evaluated after coating the plate with TRMs/PDMS metacomposites (thickness: 2.5 mm). The PEC plate was placed on the x–y plane, oriented along the positive z-axis, with Phi = 0° corresponding to the positive x-axis and Theta = 0° aligned with the positive z-axis. Radar waves incident along the -z direction. The complex permittivity of the TRMs/PDMS metacomposites was incorporated into the absorbing layer model. At 10 GHz, 3D simulations were performed with the incident wave fixed at Phi = 0° and Theta = 0°, while scattered signals were collected over various angles to comprehensively evaluate stealth performance. As shown in Fig. 6(a-d), the PEC plate coated with TRMs/PDMS exhibited markedly suppressed scattering signals compared to the uncoated PEC substrate. Among the tested composites, TRMs-2 demonstrated the most effective electromagnetic absorption and the best radar stealth performance, significantly reducing both scattering and reflection.

To further assess the practical potential of TRMs/PDMS metacomposites for radar stealth applications, a 2.5 mm TRMs/PDMS absorbing coating was applied to a military aircraft model, and its microwave absorption (MA) performance was simulated (Fig. 6(e)). The aircraft model was positioned on the x–y plane with its tail directed along the negative y-axis, where Phi = 90° corresponded to the positive x-axis and Theta = 0° aligned with the positive z-axis. Fig. 6(f-h) presents the forward RCS variation of the aircraft model under vertical polarization at 10 GHz, with the receiving angle set at Phi = 0° and Theta swept from -180° to 180°. Compared to the bare PEC aircraft model, the TRMs-2-coated model showed significantly reduced RCS across all angles. In particular, the 2D RCS profile on the x–y plane revealed a decrease from 8.41 dB·m^2 to -30.92 dB·m^2 at Theta = 0° and Phi = 0° (Fig. 6(i)). Relative to the PEC baseline, the TRMs-2 coating achieved RCS reductions of 39.33 dB·m^2, 33.86 dB·m^2, 31.27 dB·m^2, 23.11 dB·m^2, 20.93 dB·m^2, 12.47 dB·m^2, and 13.87 dB·m^2 at Theta angles of 0°, 15°, 30°, 45°, 60°, 75°, and 90°, respectively (Fig. 6(j)). These results confirm that the TRMs-2 absorbing coating substantially lowers the RCS of metallic targets, offering excellent radar stealth performance and improved survivability in military applications.

The microwave absorption mechanism of TRMs-2 is schematically illustrated in Fig. 6(k). The high-aspect-ratio TRMs units are horizontally aligned within the metacomposite, mimicking the lamellar arrangement of broadleaf plants to enable highly efficient electromagnetic wave (EMW) capture and attenuation. Upon incidence, EMW energy is collectively dissipated through a synergy of multiple pathways: the local defects in TiN/ZrO_2 fibers and oxygen-containing functional groups in RGO serve as abundant dipolar relaxation centers for strong polarization loss, while randomly distributed TiN/ZrO_2 nanoparticles and the heterointerfaces between TiN/ZrO_2 membranes and RGO drive charge separation and redistribution to amplify interfacial polarization [59]; concurrently, charge transfer under the alternating field induces micro-currents that convert EMW energy into Joule heat, providing an additional conduction-loss channel. Structurally, the electrically optimized lateral dimensions permit partial wave transmission into the interior, where cascaded multi-reflection and re-transmission among 2D planes create a “trapping effect” that prolongs interaction time and maximizes dissipation, while the discrete distribution of TRMs “leaves” effectively suppresses macroscopic in-plane currents, minimizes reflection, and ensures superior impedance matching across a broad temperature range (298–573 K). In summary, these hierarchically coupled mechanisms endow TRMs-2 with exceptional performance, systematically elucidating the pivotal role of unit-scale engineering in balancing conduction, polarization, and impedance matching, and providing a novel bioinspired strategy for next-generation high-performance microwave absorber design.

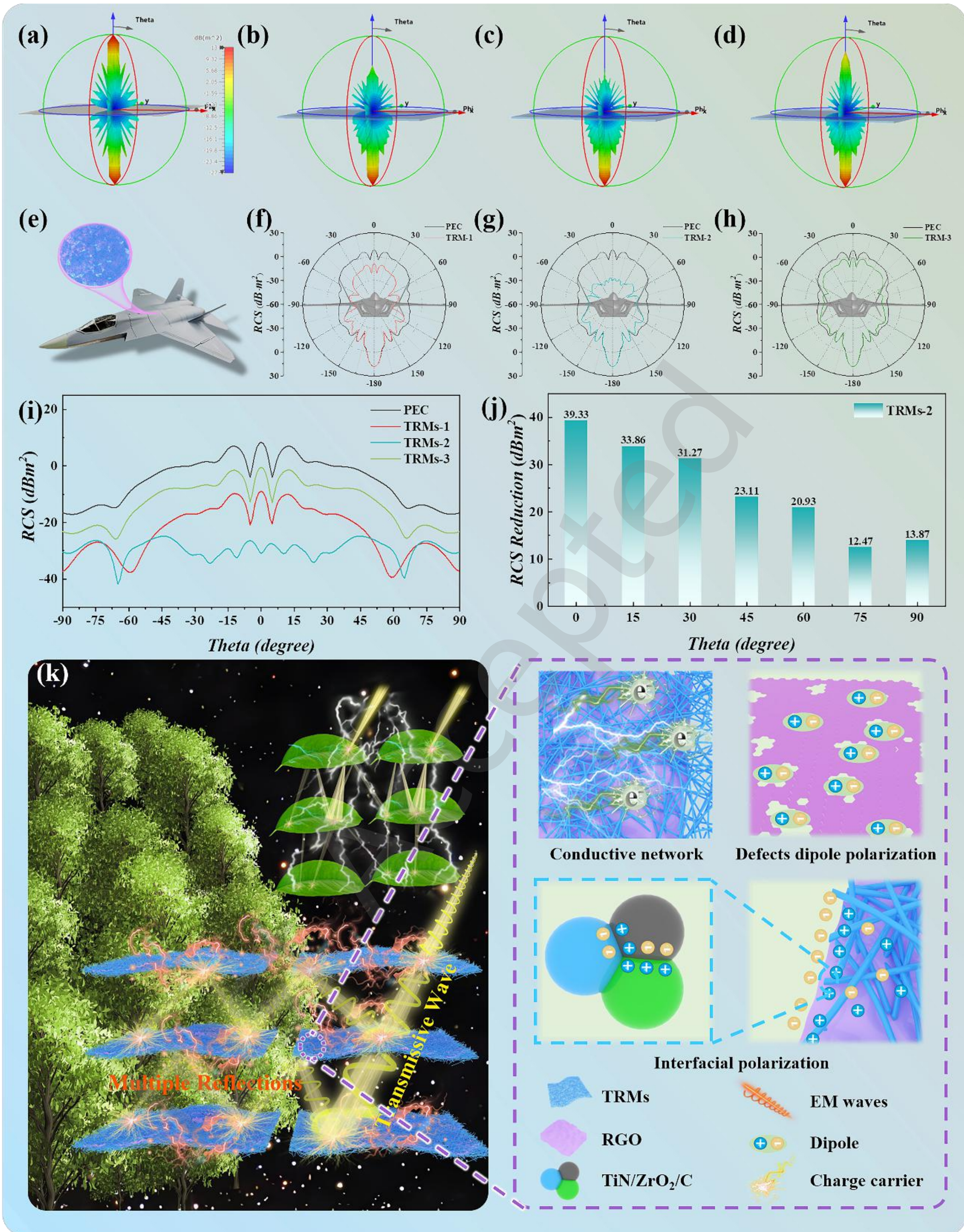

Fig. 6 Electromagnetic simulation and RCS analysis: (a-d) Far-field simulation results (CST) for PEC, TRMs-1, TRMs-2, and TRMs-3. (e) Model aircraft coated with TRMs-2. (f-i) Angular-dependent RCS simulation curves for PEC and TRMs/PDMS metacomposites. (j) RCS reduction values of TRMs-2 relative to PEC. (k) Proposed microwave absorption mechanism of TRMs-2.

4 Conclusions

Drawing inspiration from the hierarchical laminations of broadleaf foliage, this study introduces a novel metacomposite architecture utilizing 2D flexible TRMs as discrete "microwave-absorbing leaves." This biomimetic design successfully circumvents the inherent trade-off between impedance matching and dielectric loss across a broad temperature spectrum. By engineering the sub-wavelength scale geometry, we demonstrate precise command over EMW propagation modes: the planar, discrete configuration facilitates multi-scattering and cascaded attenuation, effectively switching the interaction mechanism from superficial reflection to volumetric dissipation. Crucially, by tailoring the unit lateral size (L) to the sub-wavelength regime relative to the incident wavelength (λ_m), we promote multiple internal reflections, thereby drastically enhancing electromagnetic energy conversion efficiency. Concurrently, the spatial discretization of TRMs suppresses the formation of thermally unstable conductive networks, effectively mitigating temperature-driven dielectric drift. As a result, the optimized TRMs-2 metacomposite achieves exceptional microwave absorption, featuring an RL_{min} of -57 dB (EAB of 3.8 GHz) at an ultralow filler loading of 1.1 wt.%. More importantly, it retains robust performance (EAB > 2.2 GHz) over a wide thermal range of 298–573 K. This work not only elucidates the pivotal role of 2D mesoscale geometry in governing electromagnetic dissipation but also establishes a biomimetic paradigm for next-generation, lightweight, and temperature-invariant microwave absorbers.

Electronic Supplementary Material: Supplementary material (please provide the brief detail of the ESM) is available in the online version of this article at https://doi.org/10.26599/NR.2026.94909140.

Data availability

All data needed to support the conclusions in the paper are presented in the manuscript and/or the Electronic Supplementary Material. Additional data related to this paper may be requested from the corresponding author upon request.

Acknowledgements

This work was financially supported by the National Nature Science Foundation of China (No. 22475065 and 22305066).

Declaration of competing interest

All the contributing authors report no conflict of interests in this work.

Author contribution statement

Yi Zhang: Writing - Original draft preparation, Writing - Review & Editing. Lu Zhang, Zhang Menghan: Investigation, Data curation. Yaqin Ding, Kailin Feng: Resources, Investigation. Lei Zhang: Methodology. Cuiping Li: Funding acquisition. Chunhong Gong: Conceptualization, Supervision, Project administration, Funding acquisition.

Use of AI statement

None.

References

[1] Xu, X. D.; Wang, Y. X.; Wang, C. J.; Cui, B. W., Wang, C. G. Multifunctional C/TiO_2 from MXene/Polyaniline for Electromagnetic Protection and Supercapacitor. *Energy Mater. Adv.* **2024**, *5*, 0070. https://doi.org/10.34133/energymatadv.0070

[2] Xu, H. X.; Wang, M. Z.; Hu, G. W.; Wang, S. J.; Wang, Y. Z.; Wang, C. H.; Zeng, Y. X.; Li, J. F.; Zhang, S., Huang, W. Adaptable Invisibility Management Using Kirigami-Inspired Transformable Metamaterials. *Research.* **2021**, *2021*, 9806789. https://doi.org/10.34133/2021/9806789

[3] Luo, J. Y.; Wu, L. P.; Yan, J. X.; Lv, X. T.; Luo, Y. Q.; Jiang, W.; Xiong, Z. Q.; Ni, A. Q.; Liu, C. B., Che, R. C. Radar-Stealth and Thermal-Insulating MOF-Derived Cellulose-Carbon Aerogels for Broadband Electromagnetic Wave Absorption. *Chin. Chem. Lett.* **2025**, *36(7)*, 111065. https://doi.org/10.1016/j.cclet.2025.111065

[4] Che, R. C.; Gu, J. W.; Kong, J.; Lu, W.; Huang, Y.; Wu, H. J.; Wu, G. L.; Lv, H. L.; Liu, X. F., Qi, X. S. Designing Future Nanomaterials for Electromagnetic Wave Absorption and Shielding. *Cell Rep. Phys. Sci.* **2025**, *6(3)*, 102502. https://doi.org/10.1016/j.xcrp.2025.102502

[5] Wu, Z. M.; Huang, J., Zeng, X. J. Dual Magnetic Particles Modified Carbon Nanosheets in CoFe/Co@NC Heterostructure for Efficient Electromagnetic Synergy. *Soft Sci.* **2024**, *4(4)*, 42. https://doi.org/10.20517/ss.2024.51

[6] Liu, X. J.; Duan, Y. P.; Wu, N.; Li, G. M.; Guo, Y.; Liu, J. Y.; Zhu, N.; Wang, Q.; Wang, L.; Xu, Z. C.; Wei, H.; Wang, G. J.; Zhang, Z. J.; Zhang, S. S.; Zhou, W. J.; Ma, T., Wang, T. M. Modulating Electromagnetic Genes Through Bi-Phase High-Entropy Engineering Toward Temperature-Stable Ultra-Broadband Megahertz Electromagnetic Wave Absorption. *Nano-Micro Lett.* **2025**, *17(1)*, 164. https://doi.org/10.1007/s40820-024-01638-4

[7] Si, H. X.; Zhang, Y.; Liu, Y. H.; Jiang, Z. Y.; Li, C. P.; Zhang, J.; Huang, X. X., Gong, C. H. Structural Design in Reduced Graphene Oxide (RGO) Metacomposites for Enhanced Microwave Absorption in Wide Temperature Spectrum. *J. Mater. Sci. Technol.* **2025**, *206*, 211-220. https://doi.org/10.1016/j.jmst.2024.04.011

[8] Wei, C. H.; Liu, S. H.; Wang, C. Y.; He, Z. Z.; Liu, P. B.; He, M. K., Gu, J. W. Hierarchical MnO_2 Nanosheets Decorated on Hollow Co/N-doped Carbon Toward Superior Electromagnetic Wave Absorption. *Mater. Today Nano.* **2025**, *30*, 100609. https://doi.org/10.1016/j.mtnano.2025.100609

[9] Yang, H. W.; Qiu, S. B.; Wang, L.; Li, Q. Q., Che, R. C. Heterogeneous Interface Engineering in Fe_xO_y@C@Expanded Graphite Array Structure with Confined Magnetic Coupling to Boost Microwave Absorption. *Carbon.* **2025**, *242*, 120434. https://doi.org/10.1016/j.carbon.2025.120434

[10] Li, C. P.; Zhang, L.; Zhang, S.; Yu, Q. Q.; Li, D.; Zhang, L.; Gong, C. H., Zhang, J. W. Flexible Regulation Engineering of Titanium Nitride Nanofibrous Membranes for Efficient Electromagnetic Microwave Absorption in Wide Temperature Spectrum. *Nano Res.* **2024**, *17*, 1666-1675. https://doi.org/10.1007/s12274-023-6350-2

[11] Yu, L. H.; Lian, G. J.; Zhu, G. Z.; Ren, S.; Du, Y. F.; Xiong, X. H.; Chen, R.; Zhang, J. C.; You, W. B., Che, R. C. Hollow FeCoNiAl Microspheres with Stabilized Magnetic Properties for Microwave Absorption. *Nano Res.* **2024**, *17(3)*, 2079-2087.

https://doi.org/10.1007/s12274-024-6468-x
[12] Ma, L.; Song, J. X.; Si, H. X.; Li, C. P.; Gong, C. H., Zhang, J. W. Multi-Interface Engineering in rGO/VO_2/EP Composites for Intelligent and Broadband Microwave Absorption. *J. Mater. Sci. Technol.* **2026**, *266*, 141-150. https://doi.org/10.1016/j.jmst.2025.12.005
[13] Huang, T.; Wang, D.; He, X.; Feng, Z. B.; Xiong, Z. Q.; Luo, Y. Q.; Peng, Y. H.; Luo, G. S.; Nie, X. L.; Yuan, M. Y.; Liu, C. B., Che, R. C. Coordination Thermodynamic Control of Magnetic Domain Configuration Evolution toward Low-Frequency Electromagnetic Attenuation. *Nano-Micro Lett.* **2026**, *18(1)*, 104. https://doi.org/10.1007/s40820-025-01948-1
[14] Zhao, R. Z.; Gao, T.; Li, Y. X.; Sun, Z.; Zhang, Z. Y.; Ji, L.; Hu, C. L.; Liu, X. L.; Zhang, Z. H.; Zhang, X. F., Qin, G. W. Highly Anisotropic Fe_3C Microflakes Constructed by Solid-State Phase Transformation for Efficient Microwave Absorption. *Nat. Commun.* **2024**, *15(1)*, 1497. https://doi.org/10.1038/s41467-024-45815-w
[15] Hao, B.; Chai, Z. H.; Li, M.; Duan, J. J.; Zhang, Y.; Zhang, Y. B.; Li, C. P., Gong, C. H. Design of Mesoscopic Metacomposites for Electromagnetic Wave Absorption: Enhancing Performance and Gaining Mechanistic Insights. *Soft Sci.* **2025**, *5(3)*, 39. https://dx.doi.org/10.20517/ss.2025.48
[16] Si, H. X.; Zhang, S.; Ding, Y. Q.; Chai, C. Y.; Zhou, S. S.; Li, C. P.; Zhang, J. W., Gong, C. H. Enhanced Microwave Trapping and Loss Capabilities of TiN/RGO/PDMS Metacomposites across a Wide Range of Temperatures. *Research.* **2025**, *8*, 0972. https://doi.org/10.34133/research.0972
[17] Hao, B.; Zhang, Y.; Si, H. X.; Jiang, Z. Y.; Li, C. P.; Zhang, Y. B.; Zhang, J. W., Gong, C. H. Multiscale Design of Dielectric Composites for Enhanced Microwave Absorption Performance at Elevated Temperatures. *Adv. Funct. Mater.* **2025**, *35(23)*, 2423897. https://doi.org/10.1002/adfm.202423897
[18] Si, H. X.; Zhang, Y.; Li, M.; Chai, Z. H.; Zhang, J. W.; Li, C. P., Gong, C. H. A Synergistic Design Model for Ultrathin Broadband Microwave Absorbers Using Electromagnetic Frequency Dispersion Coefficients. *Nat. Commun.* **2026**, *17*, 2991. https://doi.org/10.1038/s41467-026-69591-x
[19] An, Q.; Li, D. W.; Liao, W. H.; Liu, T. T.; Joralmon, D.; Li, X. J., Zhao, J. M. A Novel Ultra-Wideband Electromagnetic-Wave-Absorbing Metastructure Inspired by Bionic Gyroid Structures. *Adv. Mater.* **2023**, *35(26)*, 2300659. https://doi.org/10.1002/adma.202300659
[20] Wang, J. C.; Gu, S. D.; Ma, J. B.; Wu, N. B.; Chen, W.; Ma, G. J., Duan, Y. P. Bionic Interface Engineering Enables Ultrathin, Strong, and Broadband Microwave Absorbers. *ACS Appl. Mater. Interfaces.* **2025**, *17(49)*, 67187-67196. https://doi.org/10.1021/acsami.5c20652
[21] Qi, J. M.; Liang, C. B.; Ruan, K. P.; Li, M. K.; Guo, H.; He, M. K.; Qiu, H.; Guo, Y. Q., Gu, J. W. Cactus-Like Architecture for Synergistic Microwave Absorption and Thermal Management. *Natl. Sci. Rev.* **2025**, *12(11)*, nwaf394. https://doi.org/10.1093/nsr/nwaf394
[22] Xie, Y. Y.; Chen, S. C.; Wu, G., Wang, Y. Z. Leaf-Inspired Hierarchical Carbon With "Disordered Skin-Ordered Core" Architecture for Compatible Radar-Infrared Stealth. *Adv. Funct. Mater.* **2025**, *36(10)*, e17656. https://doi.org/10.1002/adfm.202517656
[23] Wang, H. Y.; Hu, P. F.; Sun, X. B.; Hou, Z. L.; Zhao, P. Y.; Zhou, L.; Yang, S. H.; Geng, C. Y.; Zhu, Y. F.; Wu, X. J., Wang, G. S. Bioinspired Disordered Aerogel for Omnidirectional Terahertz Response. *Adv. Mater.* **2025**, *37(10)*, 2418889. https://doi.org/10.1002/adma.202418889
[24] Kang, G.; Kwon, G.; Jeon, J.; Kwon, J.; Kim, M. K.; Hong, J.; Lee, A. S.; Lee, S.; Lee, B.; Kim, Y.; Lee, M.; Choi, S.; Jeong, I.; Kang, C.; Kim, D. A.; Park, H.; Joo, Y. C., Yeon, H. Electromagnetic Interference Shielding Using Metal and MXene Thin Films. *Nature.* **2025**, *647(8089)*, 356-363. https://doi.org/10.1038/s41586-025-09699-0
[25] Liu, P. B.; He, Z. Z.; Li, X. C.; Ding, L. F.; Liu, S. H., Kong, J. Multifunctional Hollow Carbon Microspheres Enable Superior Electromagnetic Wave Response and Corrosion Barrier. *Adv. Mater.* **2025**, *37(35)*, 2500646. https://doi.org/10.1002/adma.202500646
[26] Pan, F.; Wu, X. F.; Batalu, D.; Lu, W., Guan, H. T. Assembling of Low-Dimensional Aggregates with Interlaminar Electromagnetic Synergy Network for High-Efficient Microwave Absorption. *Adv. Powder Mater.* **2023**, *2(2)*, 100100. https://doi.org/10.1016/j.apmate.2022.100100
[27] Song, Z. C.; Zhu, J. F.; Wang, X. C.; Zhang, R. C.; Min, P. P.; Cao, W. X.; He, Y. R.; Han, J. C.; Wang, T. Y.; Zhu, J. Q.; Wu, L., Qiu, C. W. Origami Metamaterials for Ultra-Wideband and Large-Depth Reflection Modulation. *Nat. Commun.* **2024**, *15(1)*, 3181. https://doi.org/10.1038/s41467-024-46907-3
[28] Driscoll, T.; Basov, D. N.; Padilla, W. J.; Mock, J. J., Smith, D. R. Electromagnetic characterization of planar metamaterials by oblique angle spectroscopic measurements. *Phys. Rev. B.* **2007**, *75(11)*, 115114. https://doi.org/10.1103/PhysRevB.75.115114
[29] He, Z. Z.; Xu, H. X.; Shi, L. Z.; Ren, X. R.; Kong, J., Liu, P. B. Hierarchical $Co_2P/CoS_2@C@MoS_2$ Composites with Hollow Cavity and Multiple Phases Toward Wideband Electromagnetic Wave Absorption. *Small.* **2024**, *20(6)*, 2306253. https://doi.org/10.1002/smll.202306253
[30] Zhang, Y.; Yang, W.; Li, X., Liu, G. Design and Analysis of a Broadband Microwave Metamaterial Absorber. *IEEE Photonics J.* **2023**, *15(3)*, 1-10. https://doi.org/10.1109/JPHOT.2023.3277449
[31] Zhang, Y. H.; Li, Y.; Zhang, W.; Duan, J. J.; Zhang, Y. B.; Gong, C. H., Zhang, J. W. Ionic Liquid-Modified Reduced Graphene Oxide Aerogel With Efficient Electromagnetic Wave Absorption Capacity at Elevated Temperatures. *J. Mater. Sci. Technol.* **2027**, *283*, 203-212. https://doi.org/10.1016/j.jmst.2026.07.045
[32] Wu, Q. Q.; Ma, Z. L.; Wang, C. Y.; Tao, Y.; Wang, S. Y.; Jin, Z. Y.; Gao, T. D.; Li, C., Liu, P. B. Carbon Nanofibers with Small-Sized Co Nanoparticles and Structural Defects via a Confined-Coordination Growth Strategy Toward Electromagnetic Wave Absorption. *J. Adv. Ceram.* **2025**, *14(12)*, 9221210. https://doi.org/10.26599/JAC.2025.9221210
[33] Ding, L. F.; He, Z. Z.; Zhang, R. N.; Liu, S.; Geng, W. C., Liu, P. B. Hollow $Zn_{1-x}Co_{2-y}Ni_xFe_yO_4$ spinel via multi-metal ion doping: ultralight and broadband microwave absorber. *Soft Sci.* **2026**, *6(1)*, 2. https://doi.org/10.20517/ss.2025.113
[34] Meng, Y.; Cai, B.; Zhou, Y.; Zhou, L.; Zhang, Y.; Wang, J.; Sarula, G.; Yan, L.; Lu, M.; Liang, B., Wang, G. Bionic Coral Reef Inspired Enhanced Scattering of Trimetallic LDH Self Assembled $Ti_3C_2T_x$ MXene for Advanced Microwave Absorption. *Nano Res.* **2025**, *18(11)*, 94907842. https://doi.org/10.26599/NR.2025.94907842
[35] Liu, P. B.; Li, Y. R.; Xu, H. X.; Shi, L.; Kong, J.; Lv, X.; Zhang, J., Che, R. Hierarchical Fe-Co@TiO_2 with Incoherent Heterointerfaces and Gradient Magnetic Domains for Electromagnetic Wave Absorption. *ACS Nano.* **2023**, *18(1)*, 560-570. https://doi.org/10.1021/acsnano.3c08569
[36] Zhang, Y. L.; Zhang, Y. J.; Bai, Y. Q.; Yan, L.; Xu, G. Z.; Liu, C. Y.; Liu, X. L.; Li, X. P.; Xu, F., Ji, G. B. Synergistic Hollow Structure Design and Defect Engineering in Dandelion-Like α-MnO_2 for Superior Radar-Infrared Compatible Camouflage. *Adv. Mater.* **2026**, *38(5)*, e12477. https://doi.org/10.1002/adma.202512477

[37] Liu, X. Y.; Zhao, Y.; Zhang, Y. L.; Cui, X. C.; Xue, Y.; Lu, X. Y., Gu, J. W. Bioinspired Layered-Gradient Nanocomposites for Intelligent Electromagnetic Skins with GHz-THz Wave Absorption, Shielding, and Solvent-Driven Actuation. *Nano-Micro Lett.* **2026**, *18(1)*, 344. https://doi.org/10.1007/s40820-026-02202-y
[38] Fan, Y. H.; Cheng, H. C.; Deng, P. Y.; Wu, J. F., Zhang, B. L. Synergistic *sp-C/sp-N* Anchoring of Metal Single Atoms on Graphdiyne for Enhanced Microwave Absorption. *Nano-Micro Lett.* **2026**, *18(1)*, 345. https://doi.org/10.1007/s40820-026-02187-8
[39] Kong, X.; Zhang, S.; Pang, X.; Fu, Y.; Zhao, L., Shen, Z. Fast Design of Ultrawideband Absorbers Based on Equivalent Circuit Model. *IEEE Antennas Wirel. Propag. Lett.* **2024**, *23(6)*, 1869-1873. https://doi.org/10.1109/LAWP.2024.3371930
[40] Wang, W.; Deng, X.; Liu, D.; Luo, F.; Cheng, H.; Cao, T.; Li, Y.; Deng, Y., Xie, W. Broadband Radar-Absorbing Performance of Square-Hole Structure. *Adv. Compos. Hybrid Mater.* **2022**, *5(1)*, 525-535. https://doi.org/10.1007/s42114-021-00376-0
[41] Ming, W.; Yang, L.; Chen, H. X.; Fei, F.; Zhang, H.; Sarula, G. G.; Wang, J. H.; Wang, T. Y.; Jin, C. Z.; Liang, B. L.; Zhang, L., Yan, L. T. High Toughness MXene/ANF-CZIF67/ANF "Magnetic–Electric" Janus Film for Multifunctional Low Reflection Electromagnetic Interference Shielding. *Nano Res.* **2025**, *18(8)*, 94907621. https://doi.org/10.26599/NR.2025.94907621
[42] Zhang, K. L.; Yan, Y. F.; Wang, Z.; Ma, G. S.; Jia, D. C.; Huang, X. X., Zhou, Y. Integration of Electrical Properties and Polarization Loss Modulation on Atomic Fe–N-RGO for Boosting Electromagnetic Wave Absorption. *Nano-Micro Lett.* **2024**, *17(1)*, 46. https://doi.org/10.1007/s40820-024-01518-x
[43] He, M. K.; Zhong, X.; Lu, X. H.; Hu, J. W.; Ruan, K. P.; Guo, H.; Zhang, Y. L.; Guo, Y. Q., Gu, J. W. Excellent Low-Frequency Microwave Absorption and High Thermal Conductivity in Polydimethylsiloxane Composites Endowed by Hydrangea-Like CoNi@BN Heterostructure Fillers. *Adv. Mater.* **2024**, *36(48)*, 2410186. https://doi.org/10.1002/adma.202410186
[44] Chen, J. L.; Fan, Z. Y.; Xiong, S. X.; Huang, J.; Chen, G.; Dong, C. G., Guan, H. T. Modulation of Layer Thickness-Dependent Dielectric Polarization of $Ti_3C_2T_x$ MXene Through Moderate Ultrasonic Cavitation Effect and Water Molecule Intercalation. *Nano Res.* **2026**, *19(8)*, 94908555. https://doi.org/10.26599/NR.2026.94908555
[45] Han, Y. X.; Guo, H.; Qiu, H.; Hu, J. W.; He, M. K.; Shi, X. T.; Zhang, Y. L.; Kong, J., Gu, J. W. Multimechanism Decoupling for Low-Frequency Microwave Absorption Hierarchical Fe-Doped Co Magnetic Microchains. *Adv. Funct. Mater.* **2025**, *35(39)*, 2506803. https://doi.org/10.1002/adfm.202506803
[46] Cheng, J. Y.; Chen, Q. K.; Wang, H. H.; Jin, Y. H.; Jiang, S.; Xie, B. L.; Wang, Y. F.; Zheng, H. M.; Liu, B.; Wu, C.; Zheng, G. P., Che, R. C. Engineering Dielectric Genes in Debye Relaxation Model toward Frequency-Band-Reliant Electromagnetic Responses. *Adv. Mater.* **2026**, *38(16)*, e21471. https://doi.org/10.1002/adma.202521471
[47] Li, C. P.; Li, D.; Zhang, S.; Ma, L.; Zhang, L.; Zhang, J. W., Gong, C. H. Interface Engineering of Titanium Nitride Nanotube Composites for Excellent Microwave Absorption at Elevated Temperature. *Nano-Micro Lett.* **2024**, *16*, 168. https://doi.org/10.1007/s40820-024-01381-w
[48] Gao, T.; Zhao, R. Z.; Li, Y. X.; Zhu, Z. Y.; Hu, C. L.; Ji, L. Z.; Zhang, J., Zhang, X. F. Sub-Nanometer Fe Clusters Confined in Carbon Nanocages for Boosting Dielectric Polarization and Broadband Electromagnetic Wave Absorption. *Adv. Funct. Mater.* **2022**, *32(31)*, 2204370. https://doi.org/10.1002/adfm.202204370
[49] Liu, Z.; Xue, Y. H.; Meng, Y. T.; Wang, J. E.; Zhang, H.; Zhang, F. J.; Meng, F. B.; Zhao, B.; Yan, L. T., Liang, B. L. Reduced-Reflectance Bionic E-Skin with Electromagnetic–Environmental–Sensing Integration Enabled by Ni-Reconstructed Liquid Metal Networks. *Adv. Funct. Mater.* **2026**, *36(51)*, e76178. https://doi.org/10.1002/adfm.76178
[50] Cui, Y.; Li, C. J.; Li, R. K.; Wei, Y.; Lv, D.; Bu, J.; Wei, H., Liang, B. Effect of Synthesis Temperatures on the Composition, Microstructure, and Microwave Absorption Properties of Titanium Nitride Porous Nanofibers Prepared Using Ammonia Reduction Nitridation Process. *J. Mater. Sci.: Mater. Electron.* **2023**, *34(12)*, 1036. https://doi.org/10.1007/s10854-023-10471-1
[51] Yi, C.; Li, C. J.; Lu, J. Q.; Wei, Y. N.; Lv, D. F.; Bu, J. L.; Wei, H. Y., Liang, B. Enhanced Anti-Corrosion and Microwave Absorption Properties of Novel Binary Titanium Niobium Nitrides Nanofiber. *J. Mater. Sci.: Mater. Electron.* **2024**, *35(5)*, 337. https://doi.org/10.1007/s10854-024-12114-5
[52] Lin, X.; Gong, H. Y., Chen, Z. W. Fabrication of SiCN(Fe)/Al_2O_3 Wave-Absorbing Ceramics with Enhanced Electromagnetic Performance. *Ceram. Int.* **2023**, *49(14, Part A)*, 23851-23863. https://doi.org/10.1016/j.ceramint.2023.04.226
[53] Li, L. J.; Chao, B.; Wu, H. H.; Liu, S. K.; Fu, W. X.; Jiang, J. T.; Deng, K. X., Li, Y. Preparation of GR-TiN/PLA/TPU Composite Materials and Study on Their Microwave Absorption Properties. *Mater. Sci. Eng. B.* **2024**, *299*, 116964. https://doi.org/10.1016/j.mseb.2023.116964
[54] Ye, Z. L.; Xia, Y. C.; Luo, R. Y.; Liu, Y.; Yang, H. Y.; Ye, Z. H.; Yang, X. T.; Sun, S. Y.; Lei, B. Y., Liu, T. Y. Effect of Low-Temperature Pre-Oxidation on the Wave-Absorbing Properties of PIP-SiC/SiCN Composites. *Ceram. Int.* **2025**, *51(19, Part A)*, 27881-27894. https://doi.org/10.1016/j.ceramint.2025.04.003
[55] Fang, X.; Jin, Y. H.; Ma, H. Q.; Yin, S.; Li, T. Y.; Zhou, C.; Liu, L. Q., Zuo, R. Z. Dielectric and Electromagnetic Wave Absorption Properties of TiN/Al_2O_3 Composite Ceramics with TiN as High-Efficiency Absorbent. *Ceram. Int.* **2025**, *51(10)*, 12992-13002. https://doi.org/10.1016/j.ceramint.2025.01.145
[56] Wang, C.; Zhao, C. Q.; Peng, H. Y.; Lin, H. X.; Takáts, V.; Deng, S. F., Yao, X. G. Design and Performance Study of Ultra-High Temperature $CaMnO_3$/Polysilylaryl-Enyne Absorbing Material. *Ceram. Int.* **2024**, *50(11, Part B)*, 20421-20430. https://doi.org/10.1016/j.ceramint.2024.03.165
[57] Zhu, B.; Cui, Y.; Lv, D. F.; Xu, K. Z.; Chen, Y. J.; Wei, Y. N.; Wei, H. Y., Bu, J. L. Synthesis of Setaria Viridis-like TiN Fibers for Efficient Broadband Electromagnetic Wave Absorption in the Whole X and Ku Bands. *Appl. Surf. Sci.* **2020**, *533*, 147439. https://doi.org/10.1016/j.apsusc.2020.147439
[58] He, M. K., Gu, J. W. Tunable Low-Frequency Microwave Absorption and Thermal Management through *In-Situ* Confined Growth of Alloys within Aramid Nanofibers. *ENG. Transf. Mater.* **2026**. https://doi.org/10.2738/ENGTM.2026.0001
[59] Ren, S. Y.; Lv, G. Y.; Peng, C. X.; Yuan, S. J.; Liang, X. H.; Long, L. Y.; Man, Z. M.; Wang, D. H., Ji, G. B. Nano-Interface Engineering Enable Enhanced Dielectric Loss and Microwave Absorption Performance. *Carbon.* **2026**, *257*, 121727. https://doi.org/10.1016/j.carbon.2026.121727

Electronic Supplementary Material

2D TiN/graphene metacomposite for photosynthesis-inspired EM modulation and multi-stage attenuation

Yi Zhang, Lu Zhang, Menghan Zhang, Yaqin Ding, Kailin Feng, Lei Zhang, Cuiping Li, Chunhong Gong ✉

National & Local Joint Engineering Research Center for Applied Technology of Hybrid Nanomaterials, College of Chemistry and Molecular Sciences, Henan University, Kaifeng 475004, China

✉ Address correspondence to gong@henu.edu.cn

Supporting information to https://doi.org/10.26599/NR.2026.94909140

Address correspondence to Chunhong Gong. Firstauthor, gong@henu.edu.cn

Text S1 Calculation of the electrical dimensions of square conductive films

The fundamental relationship between wavelength λ, frequency f, and propagation speed v of an electromagnetic wave in any medium is given by:

$$v = f \cdot \lambda \quad (1)$$

In free space, the propagation speed equals the speed of light c ($c \approx 3\times10^8$ m/s), and the corresponding wavelength is denoted λ_0. Hence:

$$\lambda_0 = \frac{c}{f} \quad (2)$$

When an electromagnetic wave propagates from vacuum into a material such as silicone rubber, its phase velocity decreases. This deceleration is governed by the material's relative permittivity ε_r and relative permeability μ_r. The refractive index n of the medium is defined as[1]:

$$n = \sqrt{\varepsilon_r \mu_r} \quad (3)$$

For non- magnetic materials like silicone rubber, $\mu_r \approx 1$. The wave velocity inside the medium becomes:

$$v = \frac{c}{n} = \frac{c}{\sqrt{\varepsilon_r \mu_r}} \quad (4)$$

Substituting this expression for v into the general relation $v = f \cdot \lambda_m$ yields the general formula for the wavelength inside the medium:

$$\lambda_m = \frac{v}{f} = \frac{c}{f\sqrt{\varepsilon_r \mu_r}} \quad (5)$$

For silicone rubber, which is non- magnetic ($\mu_r \approx 1$), the formula simplifies to:

$$\lambda_m = \frac{c}{f\sqrt{\varepsilon_r}} = \frac{\lambda_0}{\sqrt{\varepsilon_r}} \quad (6)$$

This result shows that the wavelength in silicone rubber is reduced by a factor of $\sqrt{\varepsilon_r}$ compared to the free- space wavelength.

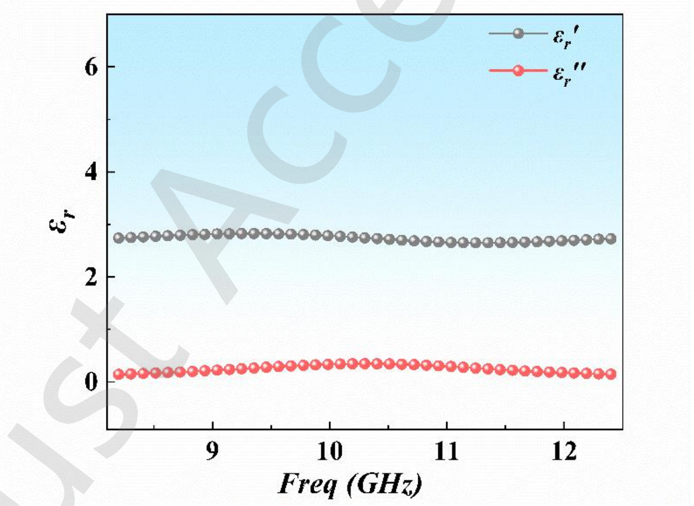

The electromagnetic parameters of the silicone rubber are shown in Fig. S1.

Fig. S1 The real and imaginary parts of the PDMS

Guided by the principle that optimal microwave absorption arises when structural dimensions approach the sub-wavelength regime, we adopt $\lambda_m/10$ as the benchmark unit size for square TiN/RGO films. Theoretical analysis indicates that at $L = \lambda_m/10$, the structure resides precisely at the critical threshold where spurious surface-wave resonances are effectively suppressed, while simultaneously achieving near-unity impedance matching with free space—thereby enabling efficient electromagnetic wave penetration, multi-scattering, and cascaded attenuation [2]. Crucially, this dimensional scale provides sufficient volumetric capacity to fully exploit the intrinsic dielectric loss of the TiN/RGO composite. Consequently, a 2 mm square unit emerges as the optimal design, striking an ideal balance between impedance matching and attenuation performance.

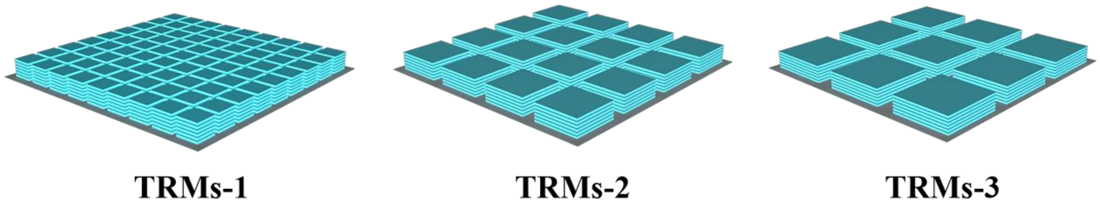

Fig. S2 The TRMs/PDMS metacomposites material model in CST

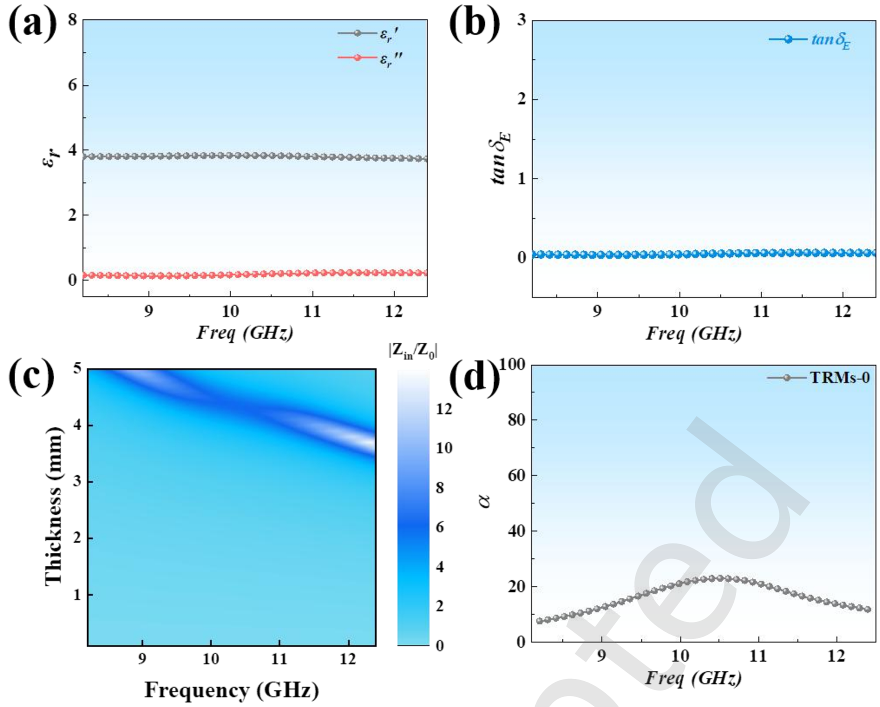

Fig. S3 (a) Real part (ε_r') and (b) imaginary part (ε_r'') of the complex permittivity, (c) normalized characteristic impedance ($|Z_{in}/Z_0|$), and (d) attenuation constant (α) of TRMs-0.

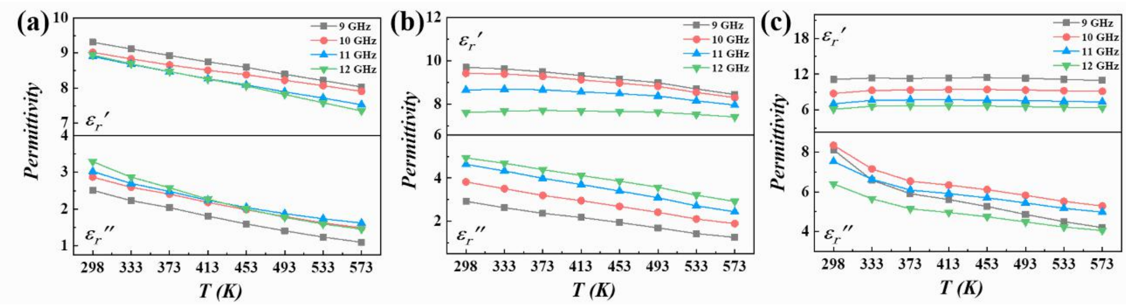

Fig. S4 The relationship between the complex dielectric constants of (a) TRMs-1, (b) TRMs-2, and (c) TRMs-3 and temperature

References

[1] Lobet, M. l.; Kinsey, N.; Liberal, I. i.; Caglayan, H.; Huidobro, P. A.; Galiffi, E.; Mejía-Salazar, J. R.; Palermo, G.; Jacob, Z., Maccaferri, N. New Horizons in Near-Zero Refractive Index Photonics and Hyperbolic Metamaterials. *ACS Photonics.* **2023**, *10(11)*, 3805-3820. 10.1021/acsphotonics.3c00747

[2] Zhang, Y.; Yang, W.; Li, X., Liu, G. Design and Analysis of a Broadband Microwave Metamaterial Absorber. *IEEE Photonics J.* **2023**, *15(3)*, 1-10. 10.1109/JPHOT.2023.3277449